Article

High-Entropy Metal Oxide (NiMnCrCoFe)$_3$O$_4$ Anode Materials with Controlled Morphology for High-Performance Lithium-Ion Batteries

Xuan Liang Wang [†] , En Mei Jin [†] , Gopinath Sahoo and Sang Mun Jeong *

Department of Chemical Engineering, Chungbuk National University, 1 Chungdae-ro, Seowon-gu, Cheongju 28644, Chungbuk, Republic of Korea
* Correspondence: smjeong@chungbuk.ac.kr
† These authors contributed equally to this work.

Abstract: High-entropy metal oxides (HEMOs) with several functional properties, including high structural stability and superior conductivity, have been recently utilized in energy-storage devices. Morphology control is the key factor to optimizing HEMO performance for successful use in lithium-ion anode materials. Hence, in this study, HEMO ((NiMnCrCoFe)$_3$O$_4$) was synthesized via a hydrothermal reaction and subsequent post-annealing process, where cetyltrimethylammonium bromide (CTAB) and urea were used to optimize the morphological structure of HEMO particles to ensure a bimodal distribution. A bimodal particle distribution of HEMO was observed and the electrochemical performance was also investigated for an anode in lithium-ion batteries (LIBs). The proposed bimodal HEMO manifests a superior electrochemical performance compared to existing HEMO, which is controlled by uniform nanoscale or micro-sized secondary particles. The present study shows that collective metal cations with different ionic radii, valence states, and reaction potentials, and a diversification of structures, enable a synergistic effect for the excellent performance of HEMOs in LIBs. The proposed HEMO shows an improved initial discharge capacity of 527 mAh g^{-1} at a high current density of 5 A g^{-1} compared to the other referred HEMO systems, and 99.8% cycle retention after 300 cycles. Further, this work allows a new approach for designing multi-element transition metal oxide anode materials using a high-entropy strategy, which can be employed in the development of advanced LIBs.

Keywords: high-entropy metal oxide; anode materials; bimodal; lithium-ion battery; high-rate performance

1. Introduction

A rapid increase in the popularity of electric vehicles and portable digital products has driven the demand for energy-storage devices with high energy density, high power density, and improved safety [1–5]. Currently, these devices mostly use lithium-ion batteries (LIBs) as energy sources, despite their limited theoretical capacity of 372 mAh g^{-1} and inability to meet high energy requirements of the near future. Therefore, the development of electrode materials with high energy density and excellent cycling and rate performance is equally important for next-generation LIBs. Various cathode materials intended for use in LIBs have been previously studied, such as LiCoO$_2$, LiFePO$_4$, LiNi$_{1-x-y}$Co$_x$Al$_y$O$_2$, and LiNi$_{1-x-y}$Co$_x$Mn$_y$O$_2$. However, little research has been conducted on anode materials, which implies that there is a greater potential to enhance the capacity of anode materials than that of cathode materials [6,7].

Recently, graphite has been widely used as a commercial anode material in LIBs, exhibiting a theoretical capacity of 372 mAh g^{-1}. To implement high-performance LIBs, it is necessary to replace graphite with new anode materials that possess a high reversible capacity [8,9]. Due to its high capacity (4200 mAh g^{-1}), silicon (Si) is used as one of the promising materials to replace graphite. However, the change in volume of the active material, of over

300% through the repeated cycle performance, affects the cycle capacity and thus limits the material's practical application [10]. Similarly, the poor electrical conductivity and huge volume expansion of phosphorous over cycling limits its practical application in LIBs, despite its high theoretical specific capacity (2596 mA h g^{-1}). Further, Baboukani et al., addressed this issue by preparing a red phosphorus-sulfurized polyacrylonitrile composite for an anode material [11]. Until now, transition metal oxides (TMOs), for example, NiO, Co$_3$O$_4$, MnO$_2$, and Fe$_2$O$_3$, have been considered as anode materials for LIBs because of their high theoretical capacities. Among these, NiO has shown a prominent advantage due to its low cost, low toxicity, high chemical stability, and high theoretical capacity (718 mAh g^{-1}) [12]. In addition, NiO anodes exhibit significant volume expansion after the lithiation process and extreme capacity fading through the cycling operation. NiO also exhibits low electronic conductivity and unfavorable electrical conductivity, thus greatly restricting its cycle stability and rate performance [13]. Co$_3$O$_4$ also has a moderately high redox capacity because it stores eight lithium atoms per molecular unit, and has thus attracted attention as a potential anode material [14,15]. Moreover, Fe$_3$O$_4$ and MnO$_2$ anodes have characteristics that exhibit high reversible capacity over a long cycle life [16,17]. Still, these TMOs commonly exhibit low conductivities, which result in significantly degraded cycle stability and speed performance. To overcome these limitations, significant effort has been focused on designing customized nanostructures and carbon composites, such as flower-like NiO/rGO nanocomposite [18], NiO/carbon aerogel microspheres [19], and hierarchical hollow pompon-like NiO carbon composite [20], to improve the conductivity. This strategy can help to improve the electrical conductivity and volume expansion, and facilitate the diffusion of Li$^+$, to some extent, but achieving a high reversible capacity after an extended charge/discharge cycle remains a major challenge. Therefore, potential anode materials for use in LIBs must exhibit excellent structural stability and electrical conductivity.

Further, numerous research plans have been reported to improve the electrochemical properties of LIBs by introducing multi-component compounds. However, cases in which the share of the doping element occupancy is too high always involve phase separation. Recent research on methods for combining various types of metals and oxide structures has therefore focused on this phenomenon. Dong et al., prepared a binary transition metal oxide Mn$_2$V$_2$O$_7$ nanosheet using the solvothermal method. The prepared nanosheet was utilized for the anode in LIBs and displayed a discharge capacity of 1096 mAh g^{-1} at 0.5 mA g^{-1} [21]. Again, VOMoO$_4$/C was synthesized through a sol-gel method by Zhao et al., which resulted in a high discharge capacity of over 830 mAh g^{-1} after 250 cycles at 0.2 A g^{-1} [22]. Additionally, Jadhav et al., prepared Mn$_{0.1}$Ni$_{0.9}$Co$_2$O$_4$/NF using the co-precipitation method for LIB applications and studied the storage performance; the preparation showed a reversible capacity of 1076 mAh g^{-1} at 1.6 A g^{-1} and excellent stability over 350 cycles [23]. It has recently been reported that high-entropy oxides (HEMOs) that contain five or more metals have the potential to overcome the obstacles described above. Some materials are classified as "high entropy" oxide with metrics based purely on entropy values resulting from the single-lattice model. In the literature, the nomenclature of these materials is not clearly defined, and they are also reported as "compositionally complex", "high entropy", and "entropy stabilized". The most general consideration is that HEMO is applied to any material hosting five or more unimolar components in which the cation and anion sublattice are simultaneously present. From the concept of high-entropy alloys (HEAs), Rost et al., developed HEMOs that then led to the emergence of high-entropy ceramics (HECs) [24]. HEMOs have attracted the interest of researchers because of their unique inherent characteristics and promising applications in various fields. Several studies on HEMOs that contain multiple metals have shown interesting thermal, dielectric, catalytic, and magnetic behaviors. HEMOs demonstrate various novel and unexpected properties, as well as the accumulation of the properties of each metal because of the inclusion of more than five different cationic metals in a single lattice. For example, the (MgCoNiCuZn)O HEMO anode exhibits excellent cycle stability, with a specific capacity of 920 mAh g^{-1} after 300 cycles at 100 mA g^{-1} [25], which was reduced to

50 mAh g^{-1} compared to its initial capacity. Furthermore, HEMO simultaneously provides a high specific capacity and long circulation stability. The $(FeCoNiCrMn)_3O_4$ HEMO reported by Wang et al., was used as an anode material in combination with transition metal ions with similar atomic radii and excellent solubility. These elements exhibited excellent electrical conductivity because of the variable valence [26]. Chen et al., prepared a spinel-structure-like $(Mg_{0.2}Ti_{0.2}Zn_{0.2}Cu_{0.2}Fe_{0.2})_3O_4$ anode material for LIBs and obtained a capacity of 504 mA h g^{-1} after 300 cycles at a current density of 100 mA g^{-1}, with high rate properties and discharge capacity of 272 mA h g^{-1} at 2000 mA g^{-1} [27]. Generally, the performance of HEMO is controlled by the type and number of metal ions present in the structure. Therefore, the particular combination of the metal ions employed is of the utmost importance. The majority of the previous studies on HEMO in LIBs focused on performance comparisons according to combinations of metal ions and ion numbers, with comparatively few studies examining shape control within the same combinations [28].

In this study, $(NiMnCrCoFe)_3O_4$ HEMO was prepared to enhance the electrochemical properties in LIBs. Ni, Co, and Fe metals have high theoretical capacities [11,14,16]; Fe and Mn show high reversible capacity characteristics over the long cycle life [16,17], and Cr not only affects the metal oxide phase but also affects the morphology [29]. $(NiMnCrCoFe)_3O_4$ HEMO was synthesized in situ via the soft-template approach to control particle morphologies with a bimodal distribution. In the synthesis process, cetyltrimethylammonium bromide (CTAB) was used as a soft template, and urea was used to produce secondary particles. This scheme produces in situ formation of a spherical soft template that employs the interaction between urea and CTAB. In addition, HEMOs that contain Ni, Mn, Cr, Co, and Fe also have cations distributed at the two Wyckoff sites of the spinel-like structure, and, therefore, various valence states are allowed and structural stabilization is also possible because of an oxygen deficiency. Further, the effect of the $(NiMnCrCoFe)_3O_4$ HEMO anode material morphology on the electrochemical performance of LIBs was comprehensively explored.

2. Materials and Methods

2.1. Materials and Synthesis of $(FeCoNiCrMn)_3O_4$ HEMO

Cobalt nitrate hexahydrate $(Co(NO_3)_2 \cdot 6H_2O$, Alfa Aesar, Spain, 99%), chromium nitrate nonahydrate $(Cr(NO_3)_3 \cdot 9H_2O$, Sigma, Spain, 99%), iron nitrate nonahydrate $(Fe(NO_3)_3 \cdot 9H_2O$, Alfa Aesar, America, 98$-$101%), manganese nitrate tetrahydrate $(Mn(NO_3)_2 \cdot 4H_2O$, Sigma, Spain, 98.5%), nickel nitrate hexahydrate $(Ni(NO_3)_2 \cdot 6H_2O$, Sigma, Germany, 98.5%), N-cetyltrimethylammonium bromide (CTAB, 99%, Samchun, Korea), and urea (Samchun, Korea) were purchased from commercial sources. Two mmol of $Co(NO_3)_2 \cdot 6H_2O$, $Cr(NO_3)_3 \cdot 9H_2O$, $Fe(NO_3)_3 \cdot 9H_2O$, $Mn(NO_3)_2 \cdot 6H_2O$, $Ni(NO_3)_2 \cdot 6H_2O$, and 1.637 mmol of urea were dissolved in 80 mL of deionized (DI) water followed by continuous stirring for several minutes. After that, 1 g of CTAB was mixed with the solution undergoing vigorous stirring. Then the solution was moved to a 100 mL Teflon-lined stainless-steel autoclave and annealed at 140 °C for 5 h for the reaction. After the hydrothermal reaction, the autoclave was cooled to room temperature, and the precipitate was collected, then washed several times with ethanol and DI water using centrifugation, before being dried in a vacuum oven at 100 °C for 12 h. Finally, the material was oxidized at 900 °C in air for 2 h at a heating rate of 10 °C min^{-1}.

The entire process is illustrated in Figure 1. For comparison, HEMOs with a uniform nanoscale particle size (HEMO1) and micro-sized secondary particles (HEMO2) with secondary particle morphology were prepared, as shown in Figure 1. These were obtained using the same procedure as that of HEMO3, although without either urea or CTAB, or only with CTAB, respectively.
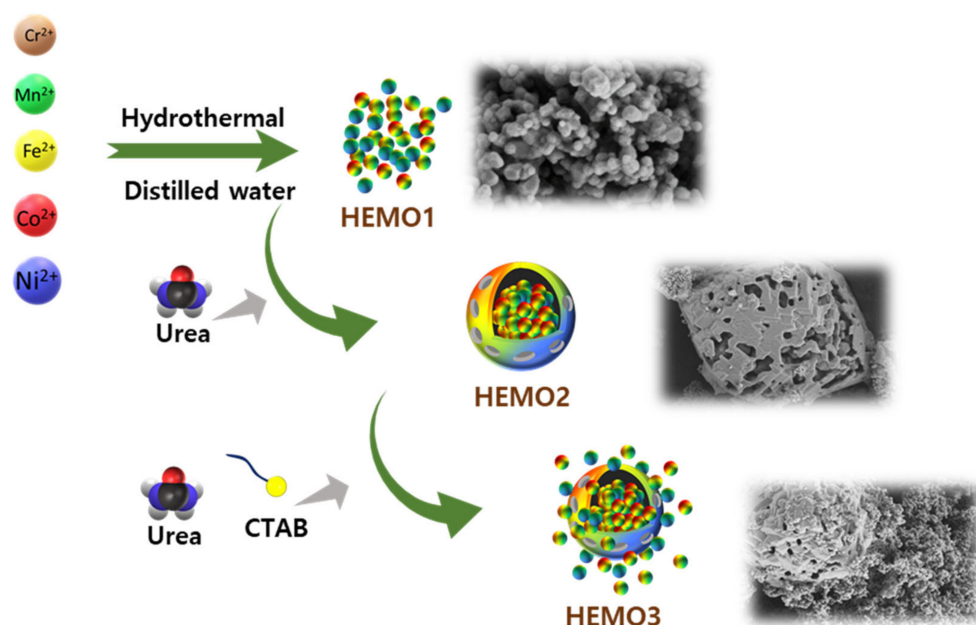
Figure 1. HEMO synthesis process. Schematic presentation of the synthesis procedure for HEMO1, HEMO2, and HEMO3.

2.2. Battery Fabrication

The HEMO anode electrode for the battery test was made by coating an optimized slurry on Cu foil using a doctor's blade. The slurry was prepared with 70 wt.% of HEMO powder, 20 wt.% of carbon black, and 10 wt.% of carboxymethyl cellulose (CMC) binder, which were dispersed in DI water. After drying the material for 1 h at 80 °C, the electrode was roll pressed and dried again under a vacuum at 110 °C for 24 h. The measured weight of the HEMO active material on Cu foil of area 2 cm^{-2} (Ø = 1.564 cm) was about 1.5 mg cm^{-2}. Then, the battery half-cell was assembled using a CR2032 coin-type cell, where Li foil and polypropylene membrane (Celgard 2400) were used as the counter electrode and separator, respectively. For electrolyte, 1 M LiPF$_6$ was used in a solution of ethylene carbonate and dimethyl carbonate at a 3:7 volume ratio, with 10% fluorinated ethylene carbonate. All the battery cells were fabricated in an Ar-filled glove box with ~0.01 ppm of oxygen and moisture level.

2.3. Material Characterization and Electrochemical Measurements

The crystalline structure of the fabricated HEMO was investigated using an X-ray diffractometer (XRD, Ultima IV, Rigaku, Japan) with Cu-Kα radiation (λ = 1.54 Å), in a 2θ angle scanning from 10 to 90° with a step time of 2° min^{-1}. The sample morphologies were characterized using a field-emission scanning electron microscopy (FE-SEM, LEO–1530, Carl Zeiss, Oberkochen, Germany) and FE-transmission electron microscopy (FE-TEM, 200KV, JEM 2100F, JEOL, Tokyo, Japan) apparatuses with selected area electron diffraction (SAED) equipment. Further, the elemental composition and chemical state were evaluated using X-ray photoelectron spectroscopy (XPS) in a PHI Quantera-II instrument (Ulvac-PHI, Chigasaki, Japan).

The electrochemical performance of the LIBs was investigated by cyclic voltammetry (CV) and galvanostatic charge–discharge (GCD) using charge–discharge test equipment (WBCS 3000 L, WonATech). The CV was carried out at a scan rate of 10 mV in a voltage range of 0.01−3.0 V, and GCD was recorded for 300 cycles in the cut-off voltage of 0.05−3.0 V (versus Li$^+$/Li) at a current density of 5 A g^{-1}. The rate capability testing was conducted from 0.1 to 5 A g^{-1}. All the measurements were carried out at 25 °C. Electrochemical impedance spectroscopy (EIS) was analyzed in the 0.01–100 kHz frequency range at a voltage perturbation of 10 mV (PGSTAT302N, Metrohm Autolab B.V.).

3. Results and Discussion

Structural crystalline quality and morphology of the anode materials are essential to reach the required high rate capability and cycling performance. The approach presented in this study involves the use of additives, such as urea and CTAB, to easily and simultaneously control particle size distribution and crystallinity. The XRD spectra representing the crystal structure of the HEMO is shown in Figure 2. The material's structural properties were not changed by the incorporation of urea or CTAB in the oxide system. The synthesized HEMO could be indexed to the *Fd-3m* space group constituting the spinel structure, which is the same as that of standard $NiMn_{0.5}Cr_{1.5}O_4$ (JCPDS card no. of 71-0855). The diffraction peaks at 18.4°, 30.2°, 35.6°, 43.2°, 57.2°, and 62.8° corresponded to the (111), (220), (311), (400), (511), and (440) crystalline planes, respectively. Further, no detectable peaks related to defects/impurities were noticed, indicating the high purity of the as-synthesized materials. The XRD spectra for HEMO2 (prepared using urea) and HEMO3 (prepared using urea and CTAB) were consistent with the results for HEMO1 (without urea and CTAB). This implies that all three samples were successfully prepared as high-entropy oxides, demonstrating that the addition of urea and CTAB did not affect the crystalline phase of the HEMO. In addition, the refined cell parameters (a = b = c) were calculated as 8.361, 8.363, and 8.365 Å for HEMO1, HEMO2, and HEMO3, respectively. These parameters match the values for spinel-$NiMn_{0.5}Cr_{1.5}O_4$ (8.366 Å). The spinel structure presents an advantage in terms of the rate capacity of an anode material by providing a 3D channel for sufficient Li^+ intercalation and extraction [30]. However, there exists a significant difference in intensity, which is a measure of crystal strength, as shown in Figure 2. The addition of urea led to an intensity value for HEMO2 that was higher than that of HEMO1 (to which nothing was added), and the crystal peak intensity of HEMO3 (containing both urea and CTAB) was the highest among the three HEMOs [31].
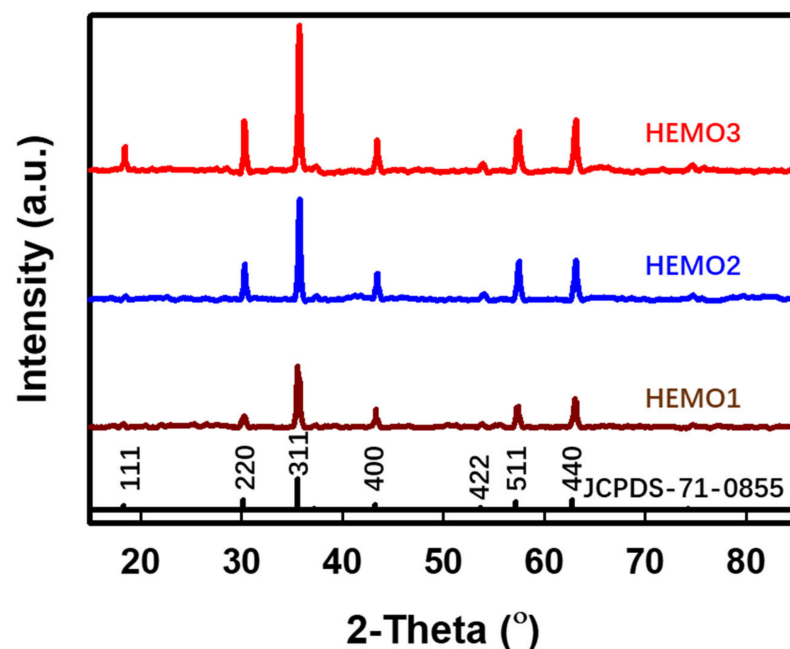

Figure 2. XRD spectra for the HEMO samples. XRD patterns for the fabricated HEMO1, HEMO2, and HEMO3 samples.

The sample morphologies were analyzed to investigate the influence of urea and CTAB on the particle size of HEMOs. Figure 3 illustrates the FE-SEM micrographs of the fabricated HEMOs with and without additional urea and CTAB. The presented morphology was consistent with what would be expected when using our experimental design. The HEMO1 (Figure 3a) sample showed a single distribution with a nanoparticle size of 200–300 nm. Further, in the HEMO2 sample in which urea was added, secondary particles of size 5–10 μm

were formed, as depicted in Figure 3b. The hollow structure is expected to exhibit excellent electrochemical properties by facilitating effective interactions with the electrolyte because of the large surface area and sufficiently spacious structure, allowing volume expansion and a short charge diffusion path for the lithium ions. In addition, the presence of secondary particles confirmed the formation of nanoparticles inside the porous shell. It is generally thought that urea forms secondary particles through the aggregation of metal ions during the hydrothermal synthesis process and that the surface is annealed during the calcination treatment process to form a porous structure. In the HEMO3 sample, a system of high-entropy metal oxide particles was formed in which large and small particles coexisted, due to the combined action of CTAB and urea (Figure 3c) [32–35]. The urea and CTAB are mainly used to optimize the morphology and structure of the prepared HEMO structure. The urea and CTAB helped the simultaneous formation of large and small particles. In addition, HEMO1, which was prepared without urea and CTAB, also confirmed that the high entropy material formation and the temperature and pressure are the driving forces of the hydrothermal reaction. Binary particle size distribution may result in the high energy density performance of LIBs and also suppress the volume expansion during the cycling process, which could lead to appropriate cycle retention [36]. In terms of electrode deformation, HEMO3 can therefore provide better properties than the other prepared samples as an anode material in LIBs. Energy-dispersive X-ray spectroscopy (EDX) elemental mapping was performed to evaluate the composition of HEMO3. It was confirmed from Figure 3d that Co, Mn, Fe, Cr, Ni, and O were well distributed within the HEMO3 particles [37,38]. Moreover, the elemental composition displayed in Figure 3e confirms that the content ratio of the five heavy metals was roughly 1:1:1:1:1 and the normalized constituent of each metal was nearly 0.2, which is consistent with our experimental design.
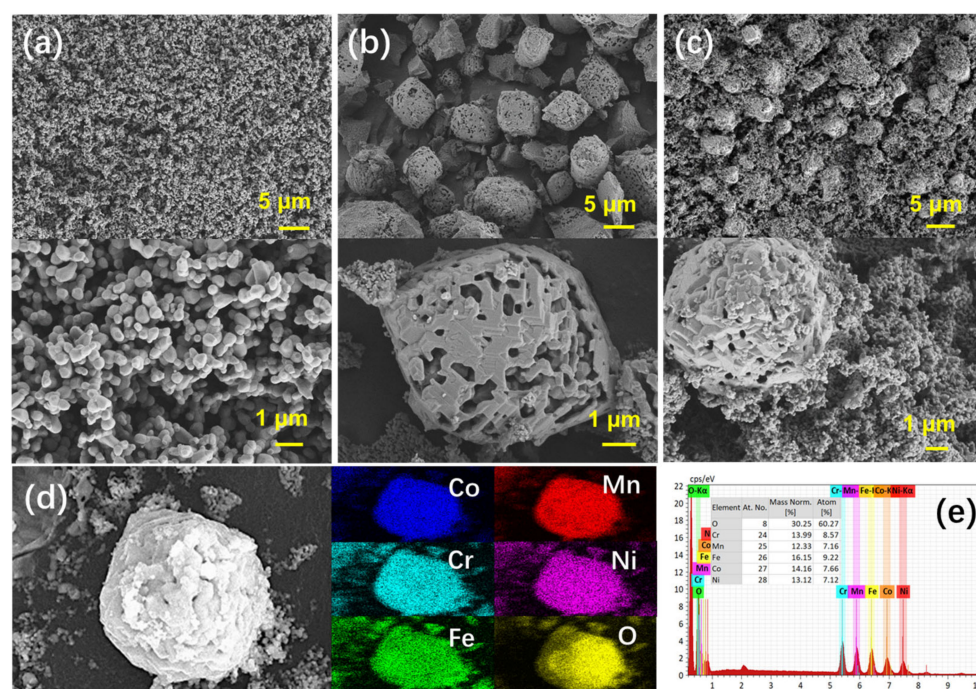

Figure 3. Images of the proposed HEMO materials. FE-SEM micrographs of (**a**) HEMO1, (**b**) HEMO2, (**c**) HEMO3 samples, and (**d**) EDX elemental mapping images of HEMO3 sample, and (**e**) composition of HEMO3 sample.

Further, the microstructural analysis of HEMO3 was performed using HR-TEM and SAED and the images are shown in Figure 4. The HR-TEM micrographs in Figure 4a display the morphology of HEMO3 correlated to the observed SEM images shown in Figure 3c. Again, the SEAD pattern shown in Figure 4b of the circular marked region in Figure 4a confirms the different concentric rings that suggest the crystallinity of the spinel structure. The diffraction rings from the outside to the inside correlate to the (622), (440), (511), (400),

(311), (220), and (111) crystal planes of HEMO3, respectively. The d-spacing values were calculated and found to be 1.26, 1.48, 1.62, 2.08, 2.48, 2.93, and 4.85 Å, corresponding to the (622), (440), (511), (400), (311), (220), and (111) spinel structure interplanar spacings, respectively. The above-obtained results correlate well with the XRD results (Figure 2) and the calculated d-value results from XRD and HR-TEM analyses are listed in Table 1. The d-spacing from XRD is calculated using the Bragg's law, $n\lambda = 2d \sin\theta$, where n is the order of diffraction, λ is the incident x-ray wavelength, and θ is the peak position. Additionally, the HR-TEM images for HEMO3 depicted in Figure 4c confirm the lattice spacing of 0.2893 nm and evidence of the (220) lattice planes in the spinel structure (PDF#JCPDS-71-0855) [39–42].
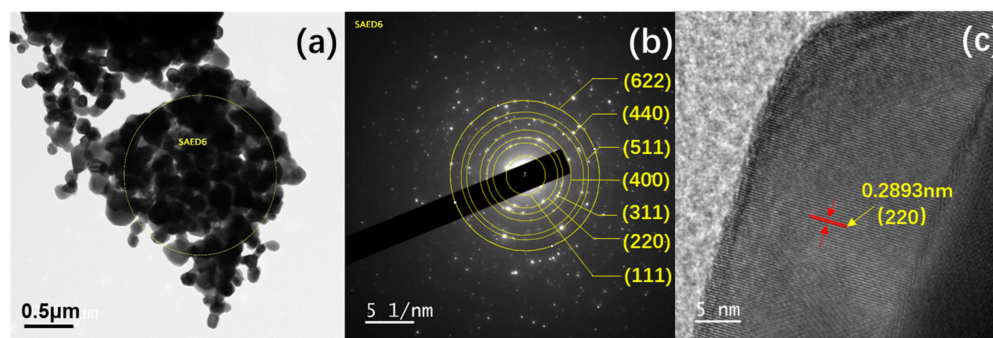

Figure 4. Images of the proposed HEMO3 material. (**a**) TEM image, (**b**) SAED pattern, and (**c**) HR-TEM image for the HEMO3 sample.

Table 1. The d-spacing values for HEMO3 obtained from XRD and HR-TEM SAED patterns.

2-Theta (°)	(hkl)	d-Spacing (Å)	
		Experimental Values from XRD	Calculated from HR-TEM
18.4	(111)	4.83	4.85
30.2	(220)	2.89	2.89
35.6	(311)	2.52	2.48
43.2	(400)	2.09	2.08
57.2	(511)	1.61	1.62
62.8	(440)	1.48	1.48
75.3	(622)	1.26	1.26

The elemental conformation and surface chemistry of the HEMO $(FeCoNiCrMn)_3O_4$ were examined by XPS. Figure 5a shows the XPS survey spectra that confirmed the presence of all the metal constituents in the synthesized HEMO. Further, Figure 5b–e depict the normalized and deconvoluted XPS spectra of Fe 2p, Cr 2p, Mn 2p, Co 2p, Ni 2p, and O 1s in their respective energy regions observed for the HEMO3 sample. As shown in Figure 5a, Fe 2p may be fitted with two spin-orbit doublets, Fe $2p_{3/2}$ and Fe $2p_{1/2}$, that appeared at binding energies 711.7 and 724.4 eV [43], respectively, accompanied by shakeup satellite peaks (719.1 and 736.2 eV). Further, Fe $2p_{3/2}$ and Fe $2p_{1/2}$ could be fitted with two peaks corresponding to two chemical states of Fe, such as Fe^{2+} and Fe^{3+} [44], with a Fe^{2+}/Fe^{3+} concentration ratio of 62.6/31.2%. For the Cr $2p_{3/2}$ spectrum, Cr^{3+} and Cr^{6+} corresponded to peaks at 577.2 and 580.3 eV, respectively [45], and Cr^{3+} was observed with a high concentration of 96.2%. The satellite peaks of Cr $2p_{3/2}$ and Cr $2p_{1/2}$ appear at 577.1 and 587.1 eV, respectively (Figure 5b). The Mn 2p spectra displayed in Figure 5c consist of two peaks at 642.7 and 654 eV, which are attributed to Mn $2p_{3/2}$ and Mn $2p_{1/2}$ spin orbits, respectively. In addition, peaks at 642.3 and 653.7 eV are related to Mn^{3+}; similarly, peaks at 644.1 and 654.4 eV are related to Mn^{4+}. Further, the deconvoluted Co and Ni 2p peaks in Figure 5d and e indicate the co-existence of Co^{2+}, Co^{3+}, Ni^{2+}, and Ni^{3+} in the respective energy regions. Figure 5f shows the normalized XPS spectra for HEMO3

in the O 1s energy region, together with the curve-fitting results. The O 1*s* spectrum may be fitted to three peaks at 529.5, 532.2, and 533.6 eV, which correspond to O^{2-} in the oxygen lattice, the metal hydroxide bond (O_v), and water, respectively. The hydroxide peaks that are apparent in the O 1s peak confirm the existence of hydroxide on the HEMO3 surface. These were detected in the Fe 2*p*, Cr 2*p*, Mn 2*p*, Co 2*p*, and Ni 2*p* spectra. In addition, peak area calculations define the contributions of O^{2-} and O_v to the O 1s spectrum for HEMO3 as 75.8 and 17%, respectively, indicating that the HEMO particles formed a stable structure. This suggests that the presence of concentrated O_v in HEMO3 can improve electron transport and electrochemical performance.
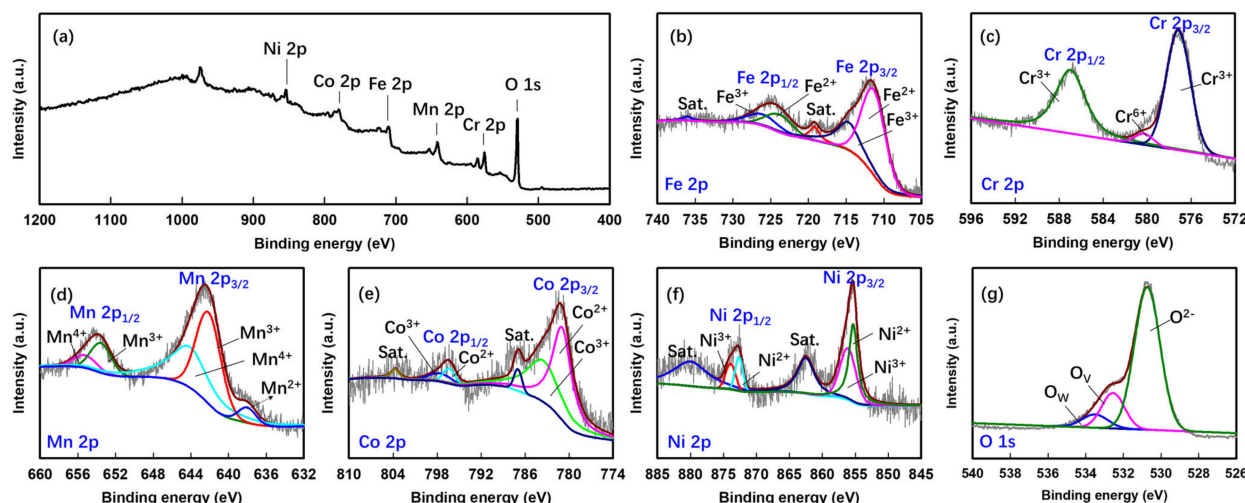

Figure 5. (**a**) XPS survey spectra for the proposed HEMO3 material. High-resolution XPS spectra for (**b**) Fe 2*p*, (**c**) Cr 2*p*, (**d**) Mn 2*p*, (**e**) Co 2*p*, (**f**) Ni 2*p*, and (**g**) O 1*s* for HEMO3.

The as-prepared HEMOs were utilized as anode materials, and their electrochemical properties were tested, to confirm their applicability in LIBs. Figure 6 shows the CV curves of different HEMOs for different cycles at a scan rate of 0.1 mV s^{-1} and within a potential range of 0.05−3.0 V. In the first negative scan, HEMO1 (with nanoparticles) showed an intense peak at 0.5 V (Figure 6a), HEMO2 (with secondary particle sizes) displayed two lithiation peaks at 0.5 and 0.25 V (Figure 6b), and HEMO3 (with bimodal particle distribution) showed three lithiation peaks at 0.77, 0.5, and 0.25 V (Figure 6c).
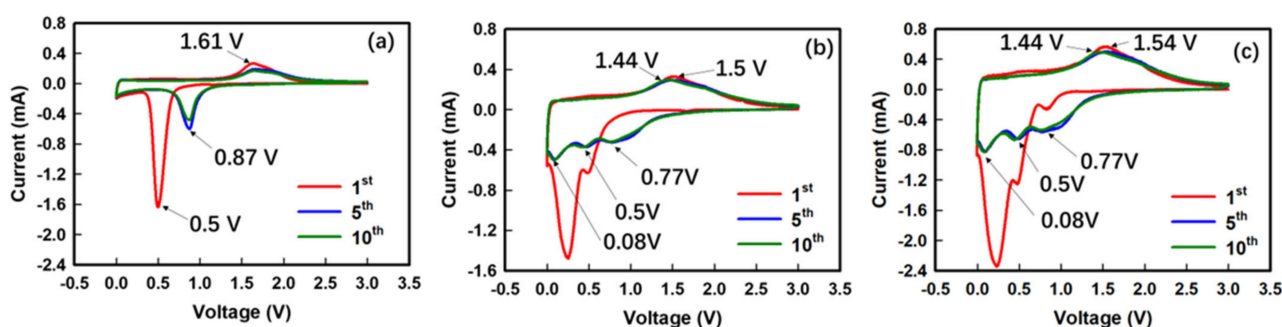

Figure 6. Cyclic voltammetry (CV) curves for the proposed HEMO anodes. CV curves for (**a**) HEMO1, (**b**) HEMO2, and (**c**) HEMO3 anodes for LIBs between 0.05 and 3.0 V, at a scan rate of 0.1 mV s^{-1}.

These lithiation peaks originated due to both the reduction of M_3O_4 (M = Fe, Co, Ni, Cr, Mn) to intermediate $Li_xM_3O_4$ and Li to form the respective metal and Li_2O matrix ($M_3O_4 \xrightarrow{Li^+} Li_xM_3O_4 \xrightarrow{Li^+} Li_2O + M$, M = Fe, Co, Ni, Cr, Mn), and further the development of a solid electrolyte interphase (SEI) [46]. In addition, the expression of two or three reduction peaks is thought to be due to differences between the intercalation rates of

lithium ions according to bimodal particle distribution. As shown in the 5th and 10th cycles, the lithiation peak potential of the HEMO1 electrode in subsequent cycles became weaker and moved to a high potential region (0.87 V), which indicates the completion of the activation process and the reduction in electrode polarization [47]. Further, the broad de-lithiation peak at 1.5 V is attributed to both the step-by-step oxidation of intermediate states to M_3O_4 and the formation of lithium ions. Moreover, the CV curves, such as those for the 5th and 10th scans, overlap well, which indicates excellent reversibility.

Figure 7a–c depict the charge/discharge curves of HEMO at a current density of 5 A g^{-1}. A voltage plateau is present at approximately 0.5 V for the first discharge cycle in the HEMO1 anode, and two and three voltage plateaus are present in the HEMO2 and HEMO3 anodes, respectively. This observation correlates well with the CV curves and confirms the metal oxide reduction and SEI layer formation. HEMO1, HEMO2, and HEMO3 showed initial specific capacities for lithiation of 476.9, 451.2, and 527.9 mAh g^{-1}, respectively, at a current density of 5 A g^{-1}. The LIB with a HEMO3 anode retained a specific capacity of 506.7 mAh g^{-1} after the 100th cycle, and showed an outstanding capacity retention of 96%. Moreover, the calculated Coulombic efficiency (CE) of the HEMO3 anode was almost 100% for all cycles, exhibiting a highly reversible chemical reaction throughout the cycling. Figure 7d displays the rate performance of the different HEMO electrodes. All samples suffered capacity decay with increasing current density. This capacity change is due to the limitations of diffusion-driven reactions at high currents during de-lithiation. Among the fabricated anodes, the HEMO3 anode delivered the best rate performance. When the capacities were calculated at a current density of 5 A g^{-1} and compared to one of 0.1 A g^{-1}, the rate of capacity retention of HEMO1, HEMO2, and HEMO3 was found to be 39, 42, and 52%, respectively. The HEMO3 electrode showed reversible capacities of 1189, 1106, 991, 880, 752, and 568 mAh g^{-1} at constant current rates of 0.1, 0.2, 0.5, 1, 2, and 5 A g^{-1}, respectively.

In particular, all the HEMO electrodes can retrieve their initial specific capacity on returning to a current rate of 0.1 A g^{-1}, which indicates their magnificent structural stability. The excellent rate capability of the HEMO could be assigned to the increase in electrical conductivity due to the presence of large oxygen vacancies confirmed from XPS analysis, which facilitates the improvement in charge transfer and storage properties [48,49]. Figure 7e shows the cycle performance of HEMO1, HEMO2, and HEMO3 anodes at a high current rate of 5 A g^{-1}. A rising trend of capacity is observed for the first few cycles for all the HEMO electrodes due to the opposition of capacity fading, and this can be assigned to the structural change and arrangement of the HEMO electrode material. Following the repeated penetration of the ions and the large activation of particles due to the interaction with the electrolyte, the number of electrochemically active components enhanced with time, which leads to the formation of a stable SEI and an increase in capacity [50,51]. The HEMO3 anode exhibited excellent specific capacity and cycling performance compared to other HEMO fabricated anodes, with a cycle retention rate of 99.8% after 300 cycles at 5 A g^{-1}. This could be described as a phenomenon caused by the binary particle size distribution and selected metal ions, indicating the possibility of applying HEMOs with a binary particle size distribution, including Fe, Co, Ni, Cr, and Mn, as anode materials for high-capacity and rate performance in LIBs.
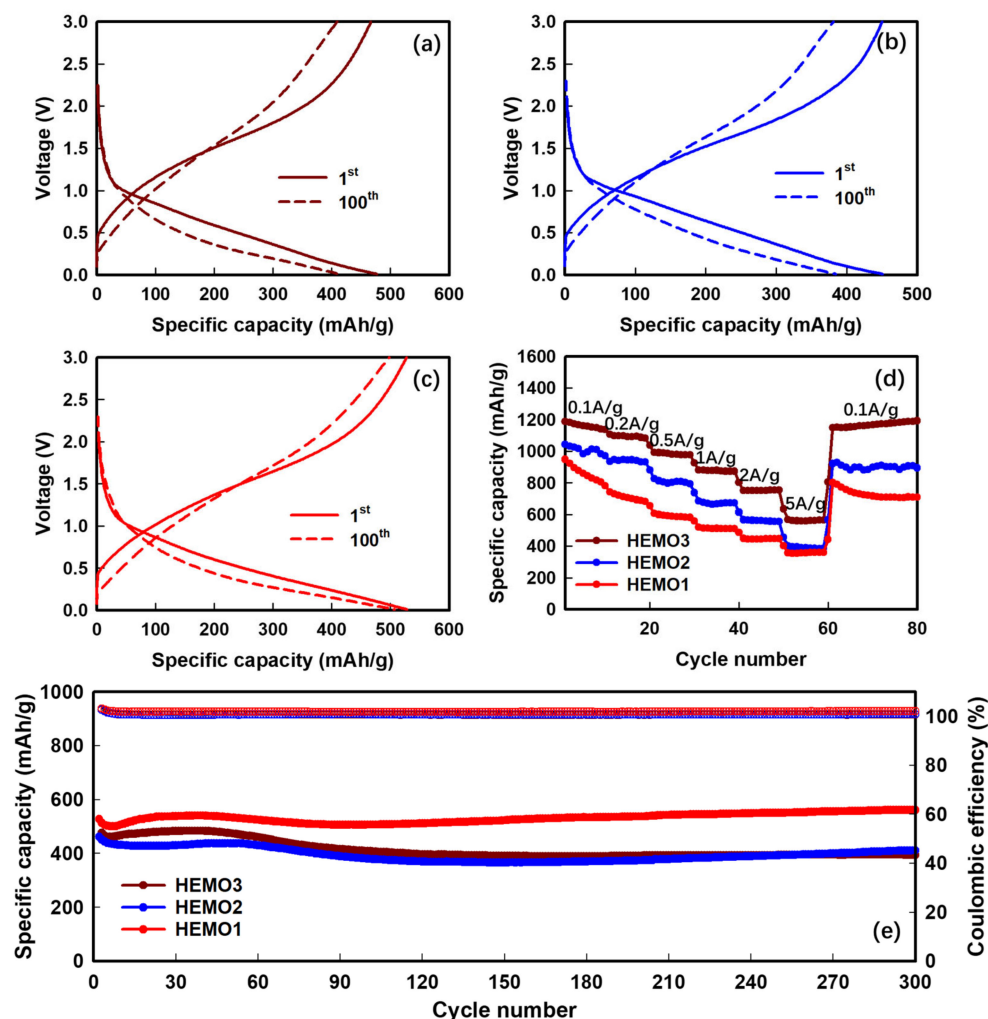
Figure 7. Electrochemical performances of different HEMO anodes used in LIBs. Charge/discharge profiles for the fabricated (**a**) HEMO1, (**b**) HEMO2, and (**c**) HEMO3 anodes at 5 A g^{-1}, (**d**) rate capabilities, and (**e**) cycle performance under 5 A g^{-1}.

The EIS measurement for the HEMO LIB half-cells was taken after 10 cycles, and the Nyquist plots fitted with equivalent circuits are shown in Figure 8a. The interface charge transfer kinetics were analyzed from the EIS spectra, by obtaining parameters such as different resistances including R_s (high-frequency region), R_{SEI} (high to medium frequency), and R_{ct} (medium frequency) referring to the bulk resistance, solid electrolyte interphase (SEI) resistance, and charge transfer resistance, respectively. The level of Li$^+$ ion diffusion on the host material is designated by the Warburg impedance (W) [52], and the constant phase element (CPE) represents the capacitance generated at the electrode surface due to the electric double layer formation [53]. The plots were fitted with an equivalent circuit (insertion diagram of Figure 8a) using the NOVA program (version 1.10.4, Metrohm Autolab B.V.) and the fitted results are listed in Table 2. It is observed that the sum of resistance R_{SEI} and R_{ct} for HEMO3 is lower than that of the other electrodes, and the two semicircles were combined and appeared as elongated semicircles in all the electrodes. The relatively low values of R_{SEI} (3.7 Ω) and R_{ct} (13.3 Ω) for the HEMO3 electrode after 10 cycles resulted in superior electrochemical properties and fast charge/electron transport during the Li$^+$ insertion/extraction reaction. Figure 8b depicts a plot of the real part of the resistance with the inverse square root of the angular speed in the low frequency determined from the slope, which is substituted using Equations (1) and (2) [54]:

$$Z' = R_s + R_{ct} + \sigma\omega^{(-1/2)} \tag{1}$$

$$D_{Li^+} = \frac{R^2 T^2}{2A^2 n^2 F^4 C^2 \sigma^2} \tag{2}$$

where Z' is the real part of the resistance, ω is the angular frequency, R is the gas constant (8.3144 kg·m^2·s^{-2}·K^{-1}·mol^{-1}), T is the absolute temperature (298.15 K), A is the surface area of the electrode (2 cm^2), n is the electronic transport ratio during redox process (1), F is the Faraday constant (96485.3321 s A mol^{-1}), C is the molar concentration of Li$^+$ in active material, and σ is the slope on the diffusion state of EIS measurement. The HEMO3 anodes show a faster D_{Li^+} (lithium ion diffusion coefficient) of 3.734×10^{-14} cm^2 than the other samples. Such enhanced electrode resistance and D_{Li^+} are thought to be the impact of the binary particle size distribution of HEMO3 and metal ions such as the selected Fe, Co, Ni, Cr, and Mn.
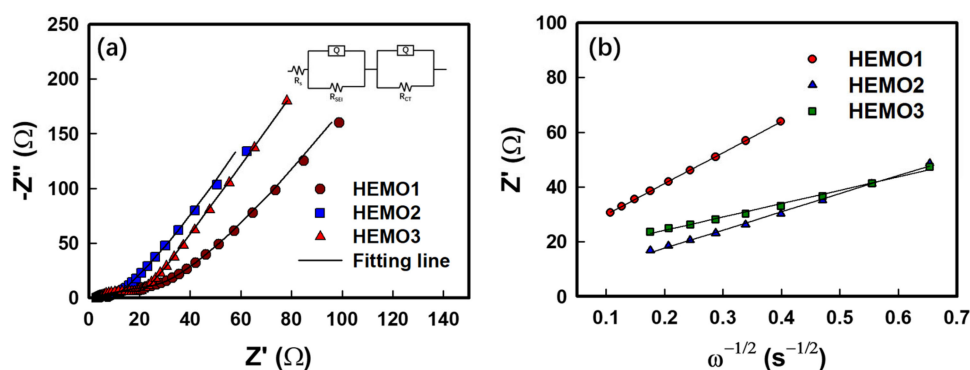

Figure 8. EIS spectra of different HEMO anodes (**a**) after 10 cycles, and (**b**) relationship between the imaginary Warburg impedance (Z') and inverse square root of angular speed ($\omega^{-1/2}$) in the low-frequency region.

Table 2. The fitting results of EIS parameters for HEMO electrodes at different cycles.

Electrodes	10th Cycle			
	R_s	R_{SEI}	R_{ct}	$D_{Li}{}^+$
HEMO1	3.2	4.8	15.8	6.852×10^{-15}
HEMO2	3.7	5.8	22.4	2.016×10^{-14}
HEMO3	3.6	3.7	13.3	3.734×10^{-14}

Moreover, the obtained specific capacity of HEMO3 is higher than the obtained values shown in the literature for high-entropy metal oxide LIB anodes. The comparison is tabulated in Table 3, and its stable capacity maintenance and high-rate characteristics are impressive [25–27,31,37,40,43,55–57]. Table 3 displays that the cycle performance results of LIBs using the HEMO are rarely observed at a high current density (>5 A g^{-1}). In particular, our (NiMnCrCoFe)$_3$O$_4$ HEMO shows an improved initial discharge capacity of 527 mAh g^{-1} at a high current density of 5 A g^{-1} compared with the (Mg, Cu, Ni, Co, Zn)O HEMO system [55]. In addition, 99.8% cycle retention was also observed after 300 cycles, which is superior to that of the widely reported HEMO systems, such as Mg$_{0.2}$Co$_{0.2}$Ni$_{0.2}$Cu$_{0.2}$Zn$_{0.2}$O, (FeCoNiCrMn)$_3$O$_4$, (CoNiZnXMnLi)$_3$O$_4$, and (Mg$_{0.2}$Ti$_{0.2}$Zn$_{0.2}$Cu$_{0.2}$Fe$_{0.2}$)$_3$O$_4$ [25–27,31,37, 40,43,55–57].

Table 3. Comparison of the electrochemical energy-storage performance achieved in this study with that of previously published work on different high-entropy metal oxide anode materials for LIBs. All cells were assessed in the voltage range of 0.01–3.0 V (Li^+/Li).

| HEMO Components (Method) | Electrochemical Measurement | | | | Refs. |
| | Discharge Capacity (C-rate) (mAh g^{-1}) | | | Cycle Retention | |
	0.1 A g^{-1}	2 A g^{-1}	5 A g^{-1}		
$Mg_{0.2}Co_{0.2}Ni_{0.2}Cu_{0.2}Zn_{0.2}O$ (Solid-state)	955	600	–	~99% (2nd–300th/0.1 A g^{-1})	[25]
$(FeCoNiCrMn)_3O_4$ (Solid-state)	586	269		~61% (2nd–300th/0.5 A g^{-1})	[26]
$(Mg_{0.2}Ti_{0.2}Zn_{0.2}Cu_{0.2}Fe_{0.2})_3O_4$ (Hydrothermal)	571	268		96.2% (800th/2 A g^{-1})	[27]
$(FeCoNiCrMnZnLi)_3O_4$ (Solid-state)	577	173		~75% (100th/0.5 A g^{-1})	[31]
$(MgCoNiZn)_{0.65}Li_{0.35}O$ (Solid-state)	925	–		~90% (30th–140th/1 A g^{-1})	[37]
$(Co_{0.2}Cu_{0.2}Mg_{0.2}Ni_{0.2}Zn_{0.2})O$ (Nebulized Spray Pyrolysis)	525	–		~94% (50th/0.2 A g^{-1})	[40]
$(Mg_{0.2}Co_{0.2}Ni_{0.2}Cu_{0.2}Zn_{0.2})O$ (Hydrothermal)	1072	500		~90% (200th/0.5 A g^{-1})	[43]
(Mg, Cu, Ni, Co, Zn)O (Green microwave-assisted method)	686	285	250	~99% (1000th/1 A g^{-1})	[55]
$(Al_{0.2}CoCrFeMnNi)_{0.58}O_{4-\delta}$ (Solution combustion synthesis)	1500	781		~40% (500th/0.2 A g^{-1})	[56]
$(CoNiZnFeMnLi)_3O_4$ (conventional solid-phase method)	665	225		~84% (100th/0.1 A g^{-1})	[57]
$((NiMnCrCoFe)_3O_4$ (Hydrothermal)	1189	752	527	~100% (300th/5 A g^{-1})	This work

To understand the fundamental reasons for the additional capacity and superior rate capability of the proposed HEMO3 material, we conducted a kinematic analysis of the electrochemical behavior through CV measurements. Figure 9a shows the CV curves of the HEMO3 electrode at different scan rates ranging from 0.1 to 1.0 mV s^{-1}; two reduction peaks and one oxidation peak are presented in the CV curves. Moreover, the peak current value of a CV curve increases with the scan speed. In general, charge storage may be represented by the capacity controlled by surface charge adsorption or chemical reactions and the diffusion control formed by Li^+ insertion/extraction kinetics. The quantitative analysis of both of the controlled reaction mechanisms was conducted from the CV data by obtaining the *b*-value, using the following equation:

$$i_{p=av^b} \tag{3}$$

$$\log(i_p) = b \log(v) + \log a \tag{4}$$

where i_p and v are the peak current and scan rate, respectively, a and b are the constant values. Figure 9b shows the log v vs. log i_p curve which obeys an exponential relationship with the scan rate v, and the *b*-values calculated from the slope of the fitted line were found to be in the range from 0.5 to 1.0. Generally, a *b*-value of 0.5 indicates a typical insertion-controlled process, and $b = 1.0$ indicates a capacitive-controlled process. For the peaks named 1, 2, and 3 in the CV of the HEMO3 electrode, the *b*-values were calculated as 0.86, 0.87, and 0.86, respectively. This demonstrates that the behavior of lithium storage in the HEMO3 electrode is mostly due to the fast surface redox reaction. The respective contribution of both processes according to the scan rate was quantitatively determined using the following equation [58,59]:

$$i(v) = k_1 v + k_2 v^{1/2} \tag{5}$$

where k_1 and k_2 are constants, and k_1v and $k_2v^{1/2}$ correspond to the capacitive effect and the insertion of diffusion control, respectively. The surface pseudocapacitive portion of the HEMO3 electrode was quantitatively calculated using the following equation:

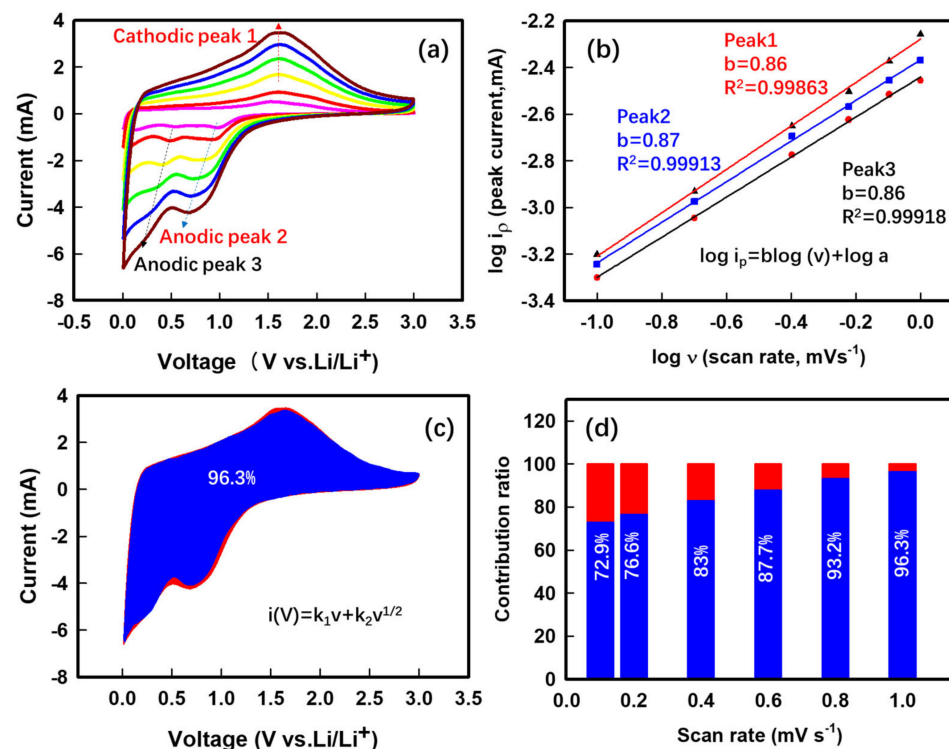$$i(v)/v^{1/2} = k_1 v^{1/2} + k_2 \qquad (6)$$

Figure 9. Charge-storage kinetics analysis of the Li$^+$ storage behavior of the proposed HEMO3 electrode. (**a**) CV curves for HEMO3 electrodes intended for LIB applications at different scan rates of 0.1 to 1.0 mV s^{-1}. (**b**) Relationship curves between the peak current and scan rate that determine b-values. (**c**) Contribution of capacitive (blue region) and diffusion (red region) at scan rate of 1.0 mV s^{-1}. (**d**) Ratio of capacitive- and diffusion-controlled percentage for the HEMO3 electrode at different scan rates.

For the HEMO3 electrode, the ratio of the capacitive contribution (blue area) was determined to be approximately 96.3% at 1.0 mV s^{-1} (Figure 9c). Figure 9d shows the contribution rate of the HEMO3 electrode capacitance control behavior at different scanning rates. The capacitive contribution increased with increasing scan rate, with capacitive contribution values of 96.3%, 93.2%, 87.7%, 83%, 76.6%, and 72.9% at 1, 0.8, 0.6, 0.4, 0.2, and 0.1 mV s^{-1}, respectively. These results suggest the good rate performance of the HEMO3 material [60,61]. The dominance of pseudocapacitive contribution confirms an excellent rate capability and is related to the stable structure of the HEMO3 material, in which Li$^+$ can easily react with the active material, thereby reducing the diffusion path resistance.

The excellent cycle and C-rate characteristics of HEMO3 could be related to a lower volume change in the particles during charging/discharging, according to the distribution effect of nanosized and binary particles and the inclusion of O_V bonds in the HEMO3 structure [62–65]. In addition, the cycle performance of the HEMO3 electrode (Figure 7e) showed that its capacity gradually increased as the cycles progressed. To determine the cause of this phenomenon, surface FE-SEM micrographs of the HEMO3 electrode were obtained in the pristine sample (before cycling, Figure 10a) and after 300 cycles (Figure 10b). After 100 cycles, large secondary particles were not observed, as shown in Figure 10b, and only small, aggregated particles were present. Further, some cracks observed in Figure 10b

may be due to the merging of small pores after continuous charge–discharge cycles or some mechanical damage during the experiment. Therefore, the stability of the HEMO3 capacity can be attributed to the aggregation of the particles that were collapsed by the SEI during the initial cycle. Figure 10c, d show the XPS spectra of the HEMO3 electrode after 100 cycles in the O 1s and Li 1s energy regions [66]. The strong peak intensity of O_V in the O 1s spectrum indicates that the particles collapsed morphologically during the cycle but were still structurally stable, which is consistent with the cycle results obtained. The presence of Li^+ peak in the Li 1*s* spectra can prove that the SEI is formed.
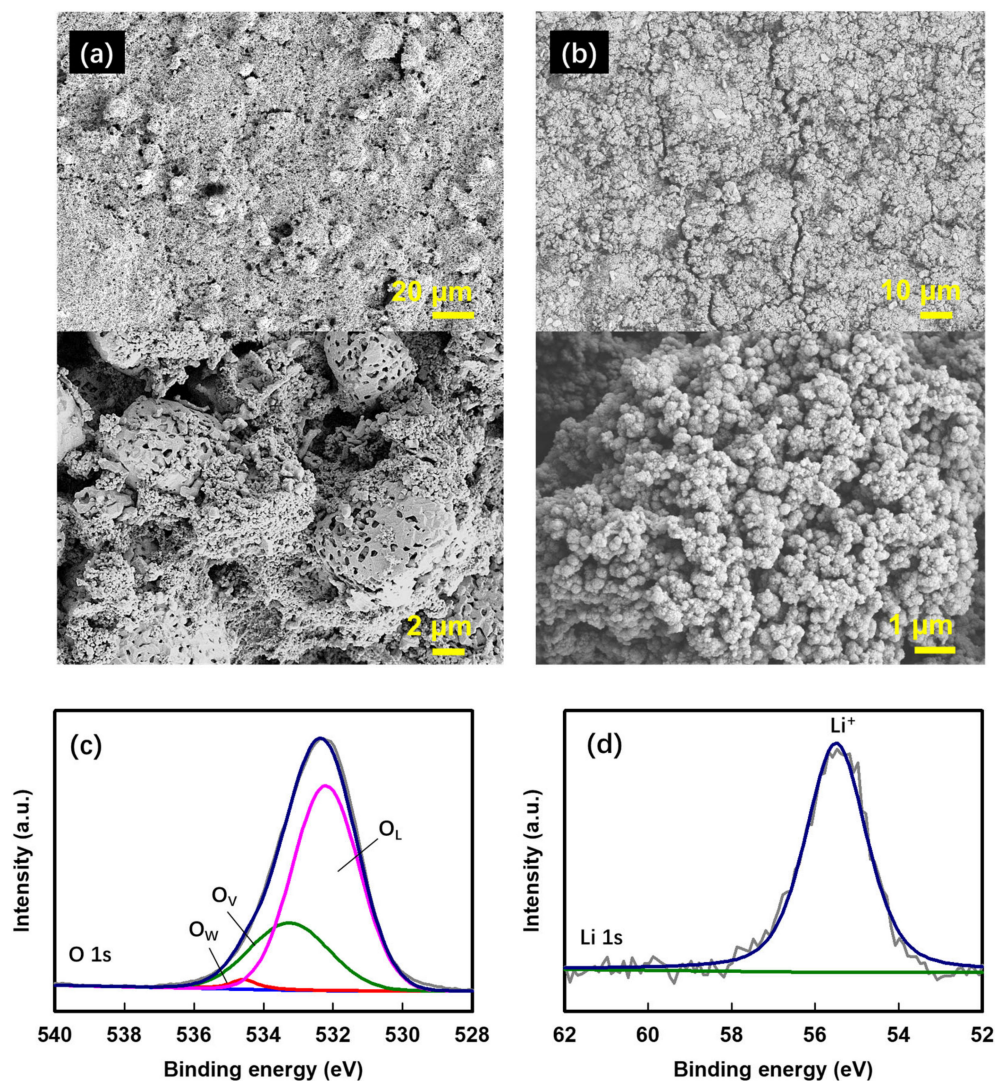

Figure 10. FE-SEM images of the proposed HEMO3 anodes. Surface FE-SEM images of the proposed HEMO3 anodes (**a**) before the cycles, and (**b**) after 100 cycles, and the high-resolution XPS spectra of (**c**) O 1s and (**d**) Li 1s energy regions for HEMO3 anodes after 100 cycles.

4. Conclusions

Increased production of electric appliances and mobile electronic devices has increased the importance of high-theoretical-capacity anode materials in LIBs. A novel high-entropy metal oxide $(FeCoNiCrMn)_3O_4$ anode material with a spinel structure was successfully synthesized using a hydrothermal reaction and followed by a post-annealing process. The binary particle distribution of the proposed HEMO3 material was successfully controlled using urea and CTAB. The proposed bimodal HEMO exhibited superior electrochemical performance compared to a HEMO controlled by uniform nanoscale or micro-scale particles. To date, LIBs with HEMOs have shown few favorable cycle performance results at high

current densities ($\geq$5 A g^{-1}), and even if they have shown favorable cycle performance results, their capacities have been considerably lower. However, compared with the existing HEMO systems, our (NiMnCrCoFe)$_3$O$_4$ HEMO shows an improved initial discharge capacity of 527 mAh g^{-1} at a high current density of 5 A g^{-1}, and 99.8% cycle retention was also shown after 300 cycles, which is superior to the widely reported HEMO systems. The outstanding electrochemical performance of (FeCoNiCrMn)$_3$O$_4$ may be attributed to the unique structure of HEMOs, their multiple mixed-valence metal elements and different cation radii, optimized electronic configuration, reduced ion diffusion resistance, and large chemical active sites. This study demonstrates an advanced method for the design of multi-element transition metal oxide cathode materials using a high-entropy approach. It also provides a direction for the application of HEMOs to reversible chemical energy storage and highlights an unexplored mechanism that should ideally be studied further in the future.

Author Contributions: X.L.W.: methodology, investigation. E.M.J.: formal analysis, writing—original draft preparation, funding acquisition. G.S.: validation, writing—review and editing. S.M.J.: conceptualization, writing—review and editing, supervision, funding acquisition. All authors have read and agreed to the published version of the manuscript.

Data Availability Statement: Not applicable.

Conflicts of Interest: The authors declare no conflict of interest.

References

1. Wen, J.; Zhao, D.; Zhang, C. An overview of electricity powered vehicles: Lithium-ion battery energy storage density and energy conversion efficiency. *Renew. Energy* **2020**, *162*, 1629–1648. [CrossRef]
2. Zheng, Q.; Watanabe, M.; Iwatate, Y.; Azuma, D.; Shibazaki, K.; Hiraga, Y.; Kishita, A.; Nakayasu, Y. Hydrothermal leaching of ternary and binary lithium-ion battery cathode materials with citric acid and the kinetic study. *J. Supercrit. Fluids* **2020**, *165*, 104990. [CrossRef]
3. Fang, F.; Chen, K.; Yin, L.; Sun, Z.; Li, F.; Cheng, H.M. The regulating role of carbon nanotubes and graphene in lithium-ion and lithium-sulfur batteries. *Adv. Mater.* **2019**, *31*, 1800863. [CrossRef]
4. Long, W.; Fang, B.; Ignaszak, A.; Wu, Z.; Wang, Y.J.; Wilkinson, D. Biomass-derived nanostructured carbons and their composites as anode materials for lithium ion batteries. *Chem. Soc. Rev.* **2017**, *46*, 7176–7190. [CrossRef] [PubMed]
5. Liu, Y.; Tang, L.B.; Wei, H.X.; Zhang, X.H.; He, Z.J.; Li, Y.J.; Zheng, J.C. Enhancement on structural stability of Ni-rich cathode materials by in-situ fabricating dual-modified layer for lithium-ion batteries. *Nano Energy* **2019**, *65*, 104043. [CrossRef]
6. Liang, C.; Gao, M.; Pan, H.; Liu, Y.; Yan, M. Lithium alloys and metal oxides as high-capacity anode materials for lithium-ion batteries. *J. Alloys Compd.* **2013**, *575*, 246–256. [CrossRef]
7. Yao, H.L.; Gao, S.S.; Fu, Z.Q.; Bao, W.C.; Cui, Z.H.; Li, Y.Q.; Xu, F.F. Encapsulating manganese oxide nanoparticles within conducting polypyrrole via in situ redox reaction and oxidative polymerization for long-life lithium-ion batteries. *Rare Met.* **2021**, *40*, 2415–2423. [CrossRef]
8. Nzereogu, P.U.; Omah, A.D.; Ezema, F.I.; Iwuoha, E.I.; Nwanya, A.C. Anode materials for lithium-ion batteries: A review. *Appl. Surf. Sci. Adv.* **2022**, *9*, 100233. [CrossRef]
9. Chen, J.; Wang, X.L.; Jin, E.M.; Moon, S.G.; Jeong, S.M. Optimization of B$_2$O$_3$ coating process for NCA cathodes to achieve long-term stability for application in lithium ion batteries. *Energy* **2021**, *222*, 119913. [CrossRef]
10. Zhang, C.; Wang, F.; Han, J.; Bai, S.; Tan, J.; Liu, J.; Li, F. Challenges and recent progress on silicon-based anode materials for next-generation lithium-ion batteries. *Small Struct.* **2021**, *2*, 2100009. [CrossRef]
11. Baboukani, A.; Khakpour, I.; Adelowo, E.; Drozd, V.; Shang, W.; Wang, C. High-performance red phospho-rus-sulfurized polyacrylonitrile composite by electrostatic spray deposition for lithium-ion batteries. *Electrochim. Acta* **2020**, *345*, 136227. [CrossRef]
12. Li, X.; Dhanabalan, A.; Wang, C. Enhanced electrochemical performance of porous NiO–Ni nanocomposite anode for lithium ion batteries. *J. Power Sources* **2011**, *5*, 9625–9630. [CrossRef]
13. Zhang, F.; Jiang, D.; Zhang, X. Porous NiO materials prepared by solid-state thermolysis of a Ni-MOF crystal for lithium-ion battery anode. *Nano Struct. Nano Objects* **2016**, *5*, 1–6. [CrossRef]
14. Hu, R.; Zhang, H.; Bu, Y.; Zhang, H.; Zhao, B.; Yang, C. Porous Co$_3$O$_4$ nanofibers surface-modified by reduced graphene oxide as a durable, high-rate anode for lithium ion battery. *Electrochim. Acta* **2017**, *228*, 241–250. [CrossRef]

15. Huang, G.; Xu, S.; Lu, S.; Li, L.; Sun, H. Porous polyhedral and fusiform Co_3O_4 anode materials for high-performance lithium-ion batteries. *Electrochim. Acta* **2014**, *135*, 420–427. [CrossRef]

16. Li, M.; Wang, W.; Yang, M.; Lv, F.; Cao, L.; Tang, Y.; Sun, R.; Lu, Z. Large-scale fabrication of porous carbon-decorated iron oxide microcuboids from Fe–MOF as high-performance anode materials for lithium-ion batteries. *RSC Adv.* **2015**, *5*, 7356–7362. [CrossRef]

17. Yu, A.; Park, H.W.; Davies, A.; Higgins, D.C.; Chen, Z.; Xiao, X. Free-standing layer-by-layer hybrid thin film of graphene-MnO_2 nanotube as anode for lithium ion batteries. *J. Phys. Chem. Lett.* **2011**, *2*, 1855–1860. [CrossRef]

18. Li, X.; Fan, L.; Li, X.; Shan, H.; Chen, C.; Yan, B.; Xiong, D.; Li, D. Enhanced anode performance of flower-like NiO/RGO nanocomposites for lithium-ion batteries. *Mater. Chem. Phys.* **2018**, *217*, 547–552. [CrossRef]

19. Guo, R.; Huang, X.; Lin, Y.; Cao, Y. NiO/Carbon aerogel microspheres with plum-pudding structure as anode materials for lithium ion batteries. *Materials* **2020**, *13*, 2363. [CrossRef]

20. Xiao, M.J.; Ma, B.; Zhang, H.; Li, X.Y.; Wang, Q.; Peng, Y.; Zhang, H.L. Hollow NiO/carbon pompons for efficient lithium ion storage. *J. Mater. Chem. A* **2022**, *10*, 21492–21502. [CrossRef]

21. Dong, X.L.; Zhang, Y.T.; Cui, C.S.; Zeng, S.Y.; Fu, C.G.; Wang, L. Study on the binary transition metal oxide $Mn_2V_2O_7$ structures for high performance lithium-ion batteries. *J. Alloys Compd.* **2022**, *907*, 164518. [CrossRef]

22. Zhao, L.; Chen, S.; Zhao, Y.; Kuang, Q.; Fan, Q.; Dong, Y. Binary metal oxide anode material, $VOMoO_4$/C, with a high capacity and ultralong cycle-life for lithium ion batteries and its multi-electron reaction mechanism. *Solid State Ion.* **2020**, *348*, 115280. [CrossRef]

23. Jadhav, H.S.; Kim, H.; Seo, J.G. Constructive designing of ternary metal oxide as an anode material for high performance lithium-ion batteries. *Int. J. Energy Res.* **2021**, *45*, 16592–16602. [CrossRef]

24. Rost, C.M.; Sachet, E.; Borman, T.; Moballegh, A.; Dickey, E.C.; Hou, D.; Jones, J.L.; Curtarolo, S.; Maria, J.P. Entropy-stabilized oxides. *Nat. Commun.* **2015**, *6*, 8485. [CrossRef]

25. Qiu, N.; Chen, H.; Yang, Z.; Sun, S.; Wang, Y.; Cui, Y. A high entropy oxide ($Mg_{0.2}Co_{0.2}Ni_{0.2}Cu_{0.2}Zn_{0.2}O$) with superior lithium storage performance. *J. Alloys Compd.* **2019**, *777*, 767–774. [CrossRef]

26. Wang, D.; Jiang, S.; Duan, C.; Mao, J.; Dong, Y.; Dong, K.; Wang, Z.; Luo, S.; Liu, Y.; Qi, X. Spinel-structured high entropy oxide $(FeCoNiCrMn)_3O_4$ as anode towards superior lithium storage performance. *J. Alloys Compd.* **2020**, *844*, 156158. [CrossRef]

27. Chen, H.; Qiu, N.; Wu, B.; Yang, Z.; Sun, S.; Wang, Y. A new spinel high-entropy oxide $(Mg_{0.2}Ti_{0.2}Zn_{0.2}Cu_{0.2}Fe_{0.2})_3O_4$ with fast reaction kinetics and excellent stability as an anode material for lithium ion batteries. *RSC Adv.* **2020**, *10*, 9736–9744. [CrossRef]

28. Wu, F.; Li, N.; Su, Y.; Shou, H.; Bao, L.; Yang, W.; Zhang, L.; An, R.; Chen, S. Spinel/layered heterostructured cathode material for high-capacity and high-rate Li-ion batteries. *Adv. Mater.* **2013**, *25*, 3722–3726. [CrossRef]

29. Pan, X.; Duan, X.; Lin, X.; Zong, F.; Tong, X.; Li, Q.; Wang, T. Rapid synthesis of Cr-doped γ-Fe_2O_3/reduced graphene oxide nanocomposites as high performance anode materials for lithium ion batteries. *J. Alloys Compd.* **2018**, *732*, 270–279. [CrossRef]

30. Sarkar, A.; Wang, Q.; Schiele, A.; Chellali, M.R.; Bhattacharya, S.S.; Wang, D.; Brezesinski, T.; Hahn, H.; Velasco, L.; Breitung, B. High-Entropy Oxides: Fundamental Aspects and Electrochemical Properties. *Adv. Mater.* **2019**, *31*, 1806236. [CrossRef]

31. Duan, C.; Tian, K.; Li, X.; Wang, D.; Sun, H.; Zheng, R.; Wang, Z.; Liu, Y. New spinel high-entropy oxides $(FeCoNiCrMnXLi)_3O_4$ (X = Cu, Mg, Zn) as the anode material for lithium-ion batteries. *Ceram. Int.* **2021**, *47*, 32025–32032. [CrossRef]

32. Shi, Y.; Zhang, M.; Fang, C.; Meng, Y.S. Urea-based hydrothermal synthesis of $LiNi_{0.5}Co_{0.2}Mn_{0.3}O_2$ cathode material for Li-ion battery. *J. Power Sources* **2018**, *394*, 114–121. [CrossRef]

33. Sha, O.; Wang, S.; Qiao, Z.; Yuan, W.; Tang, Z.; Xu, Q.; Su, Y. Synthesis of spinel $LiNi_{0.5}Mn_{1.5}O_4$ cathode material with excellent cycle stability using urea-based sol–gel method. *Mater. Lett.* **2012**, *89*, 251–253. [CrossRef]

34. Wu, X.; Zeng, M.; Wang, L.; Li, J. CTAB-assisted synthesis of $ZnCo_2O_4$ nanoparticles embedded in N-doped carbon as superior anode materials for lithium-ion battery. *J. Alloys Compd.* **2019**, *780*, 897–906. [CrossRef]

35. Ramimoghadam, D.; Hussein, M.Z.; Taufiq-Yap, Y.H. The effect of sodium dodecyl sulfate (SDS) and cetyltrimethylammonium bromide (CTAB) on the Properties of ZnO synthesized by hydrothermal method. *Int. J. Mol. Sci.* **2012**, *13*, 13275–13293. [CrossRef]

36. Chung, D.W.; Shearing, P.R.; Brandon, N.P.; Harris, S.J.; García, R.E. Particle Size Polydispersity in Li-Ion Batteries. *J. Electrochem. Soc.* **2014**, *161*, A422–A430. [CrossRef]

37. Lokcu, E.; Toparli, C.; Anik, M. Electrochemical Performance of $(MgCoNiZn)_{1-x}Li_xO$ High-Entropy Oxides in Lithium-Ion Batteries. *ACS Appl. Mater. Interfaces* **2020**, *12*, 23860–23866. [CrossRef]

38. Jin, E.M.; Kim, M.S.; Kim, T.K.; Shin, B.J.; Moon, J.H.; Jeong, S.M. Upcycling of silicon scrap collected from photovoltaic cell manufacturing process for lithium-ion batteries via transferred arc thermal plasma. *Energy* **2023**, *262*, 125447. [CrossRef]

39. Liu, X.; Huang, J.Q.; Zhang, Q.; Mai, L. Nanostructured Metal Oxides and Sulfides for Lithium-Sulfur Batteries. *Adv. Mater.* **2017**, *29*, 1601759. [CrossRef]

40. Sarkar, A.; Velasco, L.; Wang, D.; Wang, Q.; Talasila, G.; Biasi, L.D.; Kubel, C.; Brezesinski, T.; Bhattacharya, S.S.; Hahn, H.; et al. High entropy oxides for reversible energy storage. *Nat. Commun.* **2018**, *9*, 3400. [CrossRef]

41. Wang, X.L.; Chen, J.; Jin, B.; Jiang, Q.; Jin, E.M.; Jeong, S.M. Electrochemical performance of electrospun lotus–root–structure porous multichannel carbon nanotubes for lithium–sulfur battery applications. *J. Electroanal. Chem.* **2020**, *878*, 114564. [CrossRef]

42. Yan, T.; Zhong, S.; Zhou, M.; Guo, X.; Hu, J.; Wang, F.; Zeng, F.; Zuo, S. High-efficiency method for recycling lithium from spent $LiFePO_4$ cathode. *Nanotechnol. Rev.* **2020**, *9*, 1586–1593. [CrossRef]

43. Nguyen, T.X.; Patra, J.; Chang, J.K.; Ting, J.M. High entropy spinel oxide nanoparticles for superior lithiation–delithiation performance. *J. Mater. Chem. A* **2020**, *8*, 18963–18973. [CrossRef]
44. Yang, L.; Xia, Y.; Qin, L.; Yuan, G.; Qiu, B.; Shi, J.; Liu, Z. Concentration-gradient $LiMn_{0.8}Fe_{0.2}PO_4$ cathode material for high performance lithium ion battery. *J. Power Sources* **2016**, *304*, 293–300. [CrossRef]
45. Duan, C.; Li, X.; Wang, D.; Wang, Z.; Sun, H.; Zheng, R.; Liu, Y. Nanosized high entropy spinel oxide $(FeCoNiCrMn)_3O_4$ as a highly active and ultra-stable electrocatalyst for the oxygen evolution reaction. *Sustain. Energy Fuels* **2022**, *6*, 1479–1488. [CrossRef]
46. Yang, X.; Wang, H.; Song, Y.; Liu, K.; Huang, T.; Wang, X.; Zhang, C.; Li, J. Low-Temperature Synthesis of a Porous High-Entropy Transition-Metal Oxide as an Anode for High-Performance Lithium-Ion Batteries. *ACS Appl. Mater. Interfaces* **2022**, *14*, 26873–26881. [CrossRef]
47. Wang, L.; Wei, Z.; Mao, M.; Wang, H.; Li, Y.; Ma, J. Metal oxide/graphene composite anode materials for sodium-ion batteries. *Energy Storage Mater.* **2019**, *16*, 434–454. [CrossRef]
48. Somo, T.R.; Mabokela, T.E.; Teffu, D.M.; Sekgobela, T.K.; Ramogayana, B.; Hato, M.J.; Modibane, K.D. A Comparative Review of Metal Oxide Surface Coatings on Three Families of Cathode Materials for Lithium Ion Batteries. *Coatings* **2021**, *11*, 744. [CrossRef]
49. Shobana, M.K. Metal oxide coated cathode materials for Li ion batteries—A review. *J. Alloys Compd.* **2019**, *802*, 477–487. [CrossRef]
50. Li, X.; Liu, J.; Banis, M.N.; Lushington, A.; Li, R.; Cai, M.; Sun, X. Atomic layer deposition of solid-state electrolyte coated cathode materials with superior high-voltage cycling behavior for lithium ion battery application. *Energy Environ. Sci.* **2014**, *7*, 768–778. [CrossRef]
51. Ai, G.; Hu, Q.; Zhang, L.; Dai, K.; Wang, J.; Xu, Z.; Huang, Y.; Zhang, B.; Li, D.; Zhang, T.; et al. Investigation of the Nanocrystal CoS_2 Embedded in 3D Honeycomb-like Graphitic Carbon with a Synergistic Effect for High-Performance Lithium Sulfur Batteries. *ACS Appl. Mater. Interfaces* **2019**, *11*, 33987–33999. [CrossRef] [PubMed]
52. Song, B.; Lai, M.O.; Lu, L. Influence of Ru substitution on Li-rich $0.55Li_2MnO_3 \cdot 0.45LiNi_{1/3}Co_{1/3}Mn_{1/3}O_2$ cathode for Li-ion batteries. *Electrochim. Acta* **2012**, *80*, 187–195. [CrossRef]
53. Sun, Y.; Tang, J.; Zhang, K.; Yu, X.; Yuan, J.; Zhu, D.M.; Ozawa, K.; Qin, L.C. Effect of porous structural properties on lithiumion and sodium-ion storage: Illustrated by the example of a micro-mesoporous $graphene_{1-x}(MoS_2)_x$ anode. *RSC Adv.* **2021**, *11*, 34152. [CrossRef] [PubMed]
54. Lee, Y.-S.; Ryu, K.-S. Study of the lithium diffusion properties and high rate performance of $TiNb_6O_{17}$ as an anode in lithium secondary battery. *Sci. Rep.* **2017**, *7*, 16617. [CrossRef] [PubMed]
55. Kheradmandfard, M.; Minouei, H.; Tsvetkov, N.; Vayghan, A.K.; Kashani-Bozorg, S.F.; Kim, G.; Hong, S.I.; Kim, D.E. Ultrafast green microwave-assisted synthesis of high-entropy oxide nanoparticles for Li-ion battery applications. *Mater. Chem. Phys.* **2021**, *262*, 124265. [CrossRef]
56. Xiang, H.Z.; Xie, H.X.; Chen, Y.X.; Zhang, H.; Mao, A.; Zheng, C.H. Porous spinel-type $(Al_{0.2}CoCrFeMnNi)_{0.58}O_{4-\delta}$ high-entropy oxide as a novel high-performance anode material for lithium-ion batteries. *J. Mater. Sci.* **2021**, *56*, 8127–8142. [CrossRef]
57. Tian, K.H.; Duan, C.Q.; Ma, Q.; Li, X.L.; Wang, Z.Y.; Sun, H.Y.; Luo, S.H.; Wang, D.; Liu, Y.G. High-entropy chemistry stabilizing spinel oxide $(CoNiZnXMnLi)_3O_4$ (X = Fe, Cr) for high-performance anode of Li-ion batteries. *Rare Met.* **2022**, *41*, 1265–1275. [CrossRef]
58. Zhang, P.; Wang, D.; Zhu, Q.; Sun, N.; Fu, F.; Xu, B. Plate-to-Layer Bi_2MoO_6/MXene-Heterostructured Anode for Lithium-Ion Batteries. *Nano Micro Lett.* **2019**, *11*, 81. [CrossRef]
59. Chen, S.; Huang, S.; Hu, J.; Fan, S.; Shang, Y.; Pam, M.E.; Li, X.; Wang, Y.; Xu, T.; Shi, Y.; et al. Boosting Sodium Storage of $Fe_{1-x}S$/MoS_2 Composite via Heterointerface Engineering. *Nano Micro Lett.* **2019**, *11*, 80. [CrossRef]
60. Shen, L.; Lv, H.; Chen, S.; Kopold, P.; van Aken, P.A.; Wu, X.; Maier, J.; Yu, Y. Peapod-like Li_3VO_4/N-Doped Carbon Nanowires with Pseudocapacitive Properties as Advanced Materials for High-Energy Lithium-Ion Capacitors. *Adv. Mater.* **2017**, *29*, 1700142. [CrossRef]
61. Xiong, J.; Pan, Q.; Zheng, F.; Xiong, X.; Yang, C.; Hu, D.; Huang, C. N/S Co-doped Carbon Derived From Cotton as High Performance Anode Materials for Lithium Ion Batteries. *Front. Chem.* **2018**, *6*, 78. [CrossRef] [PubMed]
62. Wei, Q.; Wang, Q.; Li, Q.; An, Q.; Zhao, Y.; Peng, Z.; Jiang, Y.; Tan, S.; Yan, M.; Mai, L. Pseudocapacitive layered iron vanadate nanosheets cathode for ultrahigh-rate lithium ion storage. *Nano Energy* **2018**, *47*, 294–300. [CrossRef]
63. Sun, X.G.; Liao, C.; Baggetto, L.; Guo, B.; Unocic, R.R.; Veith, G.M.; Dai, S. Bis(fluoromalonato)borate (BFMB) anion based ionic liquid as an additive for lithium-ion battery electrolytes. *J. Mater. Chem. A* **2014**, *2*, 7606–7614. [CrossRef]
64. Delaporte, N.; Wang, Y.; Zaghib, K. Pre-treatments of Lithium Foil Surface for Improving the Cycling Life of Li Metal Batteries. *Front. Mater.* **2019**, *6*, 267. [CrossRef]
65. Dai, H.; Gu, X.; Dong, J.; Wang, C.; Lai, C.; Sun, S. Stabilizing lithium metal anode by octaphenyl polyoxyethylene-lithium complexation. *Nat. Commun.* **2020**, *11*, 643. [CrossRef]
66. Zhou, M.; Gong, J.; Deng, Z.; Lang, Y.; Zong, B.; Guo, J.; Wang, L. Synthesis and electrochemical performances of $LiNi_{0.5}Mn_{1.5}O_4$ spinels with different surface orientations for lithium-ion batteries. *Ionics* **2020**, *26*, 2187–2200. [CrossRef]